Anomalous separation of homogeneous particle-fluid mixtures: Further observations

H. S. Husain, F. Hussain, and M. Goldshtik
University of Houston, Houston, Texas 77204-4792
(Received 24 March 1994)

Previously, we reported the puzzling phenomenon of separation of components from an initially uniform mixture (air and smoke) in a rotating flow device (a cylindrical can with a rotating end disk). Here we summarize further studies of this phenomenon through experiments, analysis of particle forces, and direct numerical simulation (DNS). Separation of spherical polystyrene particles when immersed in water or pure alcohol lends further credence to the phenomenon. We have studied the dependence of the particle-free column size and its establishment time on particle size, particle concentration, disk and cylinder Reynolds numbers, and *fluid composition.* The evolution of passive markers in DNS shows segregation similar to that observed in experiments, supporting our kinematic separation hypothesis. However, kinematic action, though important, is inadequate to explain the "antidiffusion" phenomenon. Although estimates show that *known* particle forces cannot account for the particle separation, experimental results suggest the action of a yet unknown lift force whose effect is magnified kinematically in our apparatus. At high particle concentrations or when a small amount of solute (e.g. sugar, salt, or alcohol) is added to water polystyrene particle mixtures, the flow within the column becomes unstable and the particle-free column loses its axial symmetry; this unusual behavior is not yet clearly understood.

PACS number(s): 47.15.Pn, 47.55.kf

I. INTRODUCTION

A. Background

We observed the separation of smoke particles from an initially homogeneous smoke-air mixture in a rotational flow device used for vortex breakdown studies [1,2]. The apparatus, shown in Fig. 1, consists of a cylinder and top and bottom bounding disks that are hermetically sealed. The top disk (whose height H from the bottom can be adjusted) is fixed to the cylinder, and the two together are called the "can." The can and the bottom disk can be rotated independently. Unless stated otherwise, "disk" denotes the bottom disk. Thus, we study the flow in a can with a rotating lid.

To summarize our previous results [1,2], when a uniform mixture of air and smoke is placed in motion by rotating the disk only, a smoke-free vortex breakdown bubble (VB) is formed (Fig. 2). When the can is rotated in the same direction as the disk but at a lower speed, a smoke-free vortex column (VC) forms on the axis. Figures 3(a) and 3(b) show respectively an intermediate and the final state of a VC. The experiments were performed at $\mathrm{Re}_b = 2500$ and $\mathrm{Re}_c = 0$ for VB, and $\mathrm{Re}_b = 2500$ and $\mathrm{Re}_c = 1250$ for VC; in both cases $H/R = 1.8$. Here, Re_b ($\equiv \Omega_b R^2/\nu$) and Re_c ($\equiv \Omega_c R^2/\nu$) are the Reynolds numbers of the bottom disk and the can based on their angular velocities Ω_b and Ω_c; ν is the kinematic viscosity, and R and H are the radius and height of the chamber. The formation of the smoke-free column is complete within 50–70 s at a slow rotational speed of 2–3 rev/s. This is also the establishment time of the VB or VC. Such rapid particle separation (at low rotation rates) led us to believe that this phenomenon is due to predominantly kinematic rather than dynamic effects.

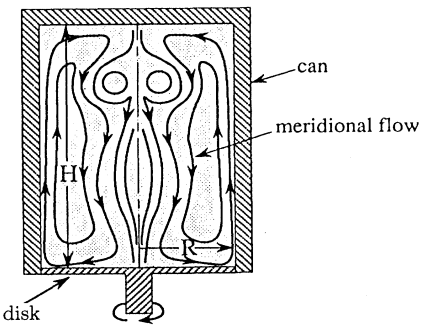

FIG. 1. Schematic of the flow facility, where meridional streamlines are shown for an axisymmetric vortex breakdown bubble.

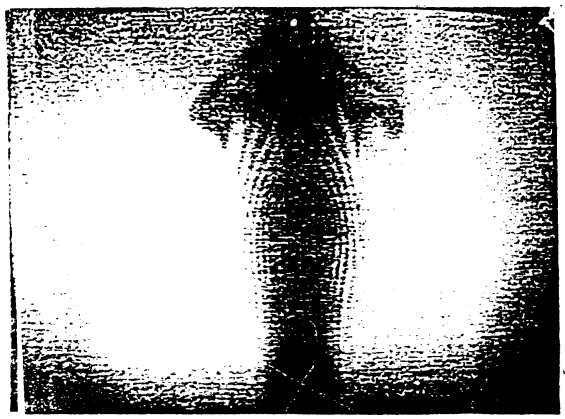

FIG. 2. Flow visualization picture showing smoke separation in the axisymmetric vortex bubble for $\mathrm{Re}_b = 2500$ at $t = 70$ s.

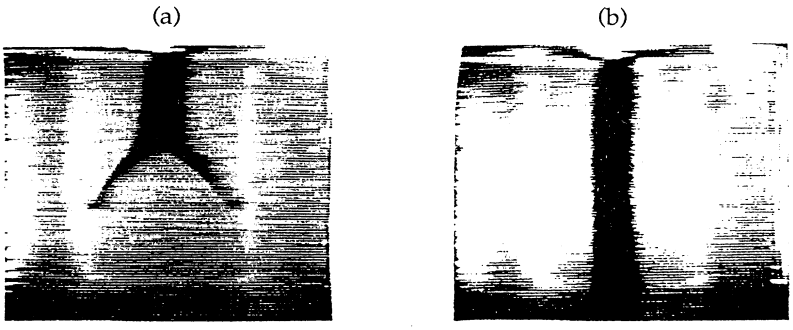

FIG. 3. Flow visualization picture showing smoke separation in the column vortex for $Re_b = 2500$ and $Re_c = 1250$. (a) $t = 30$ s; (b) $t = 75$ s.

B. Motivation

Our results raised questions regarding the validity of particle separation by kinematic effects. Some have suggested that the separation of particles must be a dynamic effect since an initially uniform smoke distribution should otherwise remain so forever. Experiments, numerical simulations, and particle force estimates reported here further explore this phenomenon.

Known forces describing fluid-particle interaction seem too weak to be important in this process. Experiments to specifically evaluate the role of the largest forces, i.e., gravity and inertial forces, in the process are detailed in Sec. II. In Sec. III, direct numerical simulation (DNS) results and analysis are presented for the kinematic separation of massless markers. Our previous experiments have been extended to include liquids (e.g., water, pure alcohol, water-alcohol solution, sugar-water solution, and salt-water solution) seeded with spherical polystyrene particles. Section IV presents results on the effect of particle size d, particle concentration c (number of particles per unit volume), Re_b, Ω_b/Ω_c, and fluid composition. Conclusions are given in Sec. V. Estimates of particle forces and details of the numerical simulations are given in Appendices A and B, respectively.

II. EFFECT OF FORCES: EXPERIMENTAL EVIDENCE

It may appear that the depletion of particles near the wall is a trivial consequence of the migration of particles across streamlines in the presence of the wall, velocity profile curvature, and other known forces (e.g., Stokes, gravity, centrifugal, Mangus, etc.) acting on the particles. However, for very small particles, which almost follow the streamlines (i.e., very small relative velocity between a particle and the fluid), the effect is negligible [3]. The particles we used are too small to undergo any significant displacement from the wall by the action of the known forces. To understand the particle depletion mechanism, we carefully performed experiments and also estimated the effects of various forces. Experimental verifications of the effects of gravity and inertial forces are elaborated in this section, while the estimates of other forces are given in Appendix A.

In the experiments, the initially uniform smoke-air mixture was achieved in three ways: (i) leaving the mixture at rest for a sufficiently long period, (ii) establishing solid-body rotation (by rotating the can and the disk at the same speed in the same direction), and (iii) rotating the two in opposite directions. Once the uniform state was established, the desired can and disk rotation rates were set and time counted from that instant. Experiments were also conducted with initially nonuniform particle distributions. In all cases, the final particle-depleted column or bubble was independent of the initial particle distribution.

Experiments confirm that gravity and inertial forces play no role in the phenomenon.

A. Role of gravity

Estimates of particle forces (Appendix A) that cause particle separation reveal that the largest relevant forces in a smoke-air mixture are Stokes drag and gravity (smoke particles are abut 1000 times heavier than air). It follows that if gravity were significant in forming particle-free fluid, separation should start from the top of the can. Whereas unfiltered smoke showed significant settling within 10–15 min due to a wide range of particle sizes, smoke filtered through fine cotton remained uniformly distributed throughout the domain undergoing random (Brownian) motion even after 24 h, implying that the particles are very small and that gravity effects can be neglected. Direct measurement of smoke particles using an electron microscope (500 000 amplification) confirmed the size to be less than 0.1 μm and revealed their irregular cornflakelike shape (Fig. 4). Considering only gravity, 0.1-μm smoke particles should sink through a distance of about 3 cm in 24 h.

We verified the effect of gravity by rotating the top disk only (configuration 2). In this case, a smoke-free (inverted) VB is formed similar to that shown in Fig. 2 (configuration 1). If gravity were causing separation at

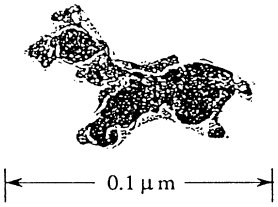

FIG. 4. A typical smoke particle captured by the electron microscope.

the top of the facility, the clear fluid formed would be advected into the bubble forming the particle-free VB. Since for configuration 2, the distance traversed by this clear fluid layer would be three times longer than for configuration 1, the establishment time should be about three times greater for $H/R=1.8$. However, in both configurations, the particle-free VB establishment times were the same, confirming the conclusion that gravity is not the dominant factor.

B. Role of centrifugal force

The simplest way to estimate the role of centrifugal acceleration is to rotate the can and the disk together at the same speed Ω. When the steady state is reached, the fluid-particle mixture attains solid-body rotation. If centrifugal forces were dominant, particles would move radially outward everywhere, producing separation as in a conventional centrifugal separator. Such solid-body rotation of the fluid mixture did not reveal any separation of practices even after 30 min. However, a small difference $(\Omega_b-\Omega_c)$ in the rotational speeds of the can and the disk initiated particle separation immediately.

To examine the effect of centrifugal forces along the axis of VC where the streamlines converge at the top (concentrating angular momentum) and spiral downward, we inserted tubes of various diameters (0.317, 0.635, and 0.952 cm) along the axis. The role of the tube was to prevent collapse of flow swirl near the axis and, hence, reduce the centrifugal acceleration. The cross-sectional area of the particle-free column and the establishment time remained roughly the same with or without the tube, demonstrating that centrifugal forces due to vortex collapse on the axis play no significant role in the separation process.

We examined the effects of meridional acceleration a_m (related to the curvature of the meridional flow; see Appendix A) in two ways: (i) instead of rotating the entire bottom disk, a smaller disk (7.62 cm in diameter), inserted inside the bottom disk (15.24 cm in diameter), was rotated [Fig. 5(a)]; and (ii) the flat bottom disk was replaced by a disk with rounded corners [of radius 1.27 cm; see Fig. 5(b)]. Both modifications decreased the curvature of meriodional streamlines near the bottom corner, thereby reducing a_m. In a third configuration, both top and bottom disks with rounded corners were used [Fig. 5(b)]. None of the configuration changes produced any difference in the separation characteristics, thus confirming that meridional acceleration also does not play a dominant role.

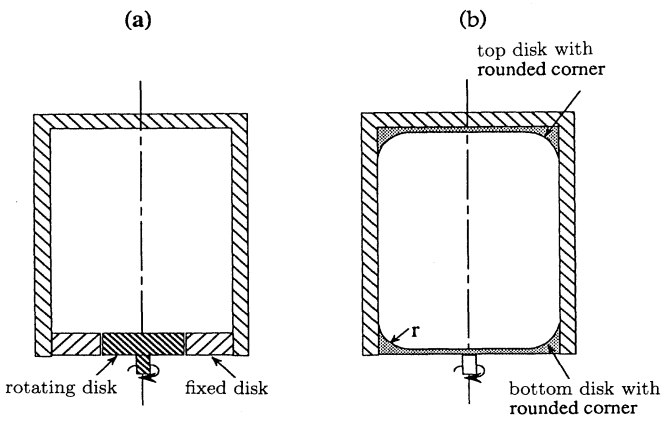

FIG. 5. Schematics of modified facility to reduce meridional acceleration.

III. NUMERICAL SIMULATION

A. Numerical approach

A kinematic separation hypothesis was previously proposed [1,2] as a tentative explanation: the particles are considered to be "frozen" markers following the flow, and the kinematics of *discrete* markers produces the observed separation phenomenon. This hypothesis has been examined using the trajectories of massless markers obtained via direct numerical simulation of the flow field.

Axisymmetric flow simulations were performed on a 200×360 grid in the meridional plane. Three types of initial marker distributions were studied: (i) regular homogeneous, (ii) random homogeneous, and (iii) a distribution following $c'\propto r$, where c' is the "planar" particle concentration (see Appendix B). Regular homogeneous and random homogeneous marker distributions refer to the placement of a marker at the center and at a random location inside each square cell, respectively, in the meridional plane. Numerical simulation methods and the justification of initial marker distributions are described in Appendix B.

B. Simulation results

Calculations were performed for Re_b $(\equiv\Omega_b R^2/\nu)=2500$, $H/R=1.8$, and $\Omega_b/\Omega_c=0.5$, consistent with the parameters used in experiments using smoke-air mixtures. The fluid was assumed to be at rest at $t=0$. Time evolution for 49×89 markers with initially regular homogeneous and random homogeneous distributions is shown in Figs. 6(a) and 6(b). The corresponding instantaneous meridional streamlines (i.e., intersections of stream surfaces with the meridional plane) are shown in Fig. 6(c); the first panel of Fig. 6(c) corresponds to $t=0.01$ s. Each disk acts as a Karman pump to drive the fluid radially away from the axis and then along the cylinder wall. During transition, the streamlines show two cells [e.g., at $t=0.01$ and 8 s in Fig. 6(c)]; a smaller cell develops near the top and a larger cell near the bottom. The flow driven by the bottom and top disks produces anticlockwise and clockwise circulatory motions, respectively, in the meridoinal plane; the corresponding streamlines are denoted by solid and dashed lines. The descending and ascending flows first meet along the wall and are then directed radially inward, causing flow separation on the cylinder wall [point A in Fig. 6(c) at $t=8$ s]. With increasing time, the flow separation location moves upward

because the ascending flow velocity generated by the faster-rotating bottom disk is greater than that produced by the top disk. Gradually, the two-cell streamline pattern becomes a one-cell structure (obvious at $t=24$).

Note that the streamlines produced by the ascending flow deviate from the cylinder wall. Simultaneously, the trajectories of discrete markers deviate from the wall, producing a marker-free fluid layer adjacent to the wall. The marker-free fluid then advects into the layer between the separated streamlines of the clockwise and anticlockwise motions, producing a marker-depleted layer [resembling a "shoulder," which is indicated by arrows in Fig. 6(a) and 6(b) at $t=24$ and 40 s]. As the anticlockwise circulatory motion overcomes the clockwise motion, the marker-depleted layer between the two circulatory motions moves first toward the upper corner, then radially inward. Simultaneously, the particles near the axis at the top are driven downward and the central column is occupied by the advecting clear fluid from the boundary layer, eventually completing the marker-free column.

In the simulation with a random homogeneous marker distribution, although the marker distributions are different, the steady-state column is almost identical to that of the regular homogeneous marker distribution case.

Time evolution of 49×89 markers for the initial state $c'=Ar$ is depicted in Fig. 7. Note that, although there are no markers near the top (up to about $r/R=0.15$) at $t=0$, inward radial motion near the top moves the markers close to the axis ($t=8,24$); such initial inward marker

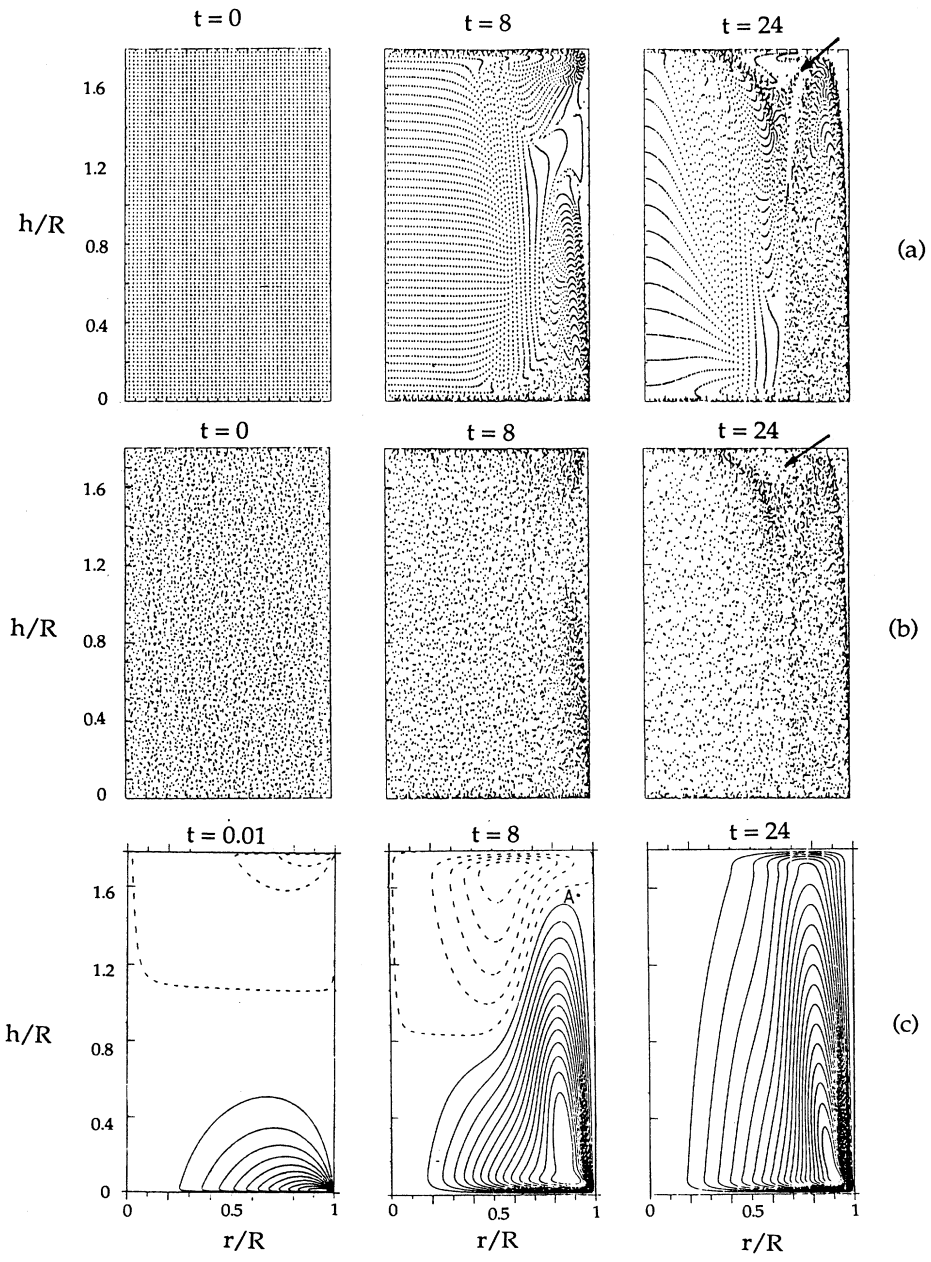

FIG. 6. Numerical simulation results showing time evolution of trajectories of 49×89 markers. (a) Trajectories for initially regular homogeneous marker distribution; (b) trajectories for initially random homogeneous marker distribution; and (c) instantaneous meridional streamlines (dashed lines correspond to negative stream functions). $Re_b=2500$, $Re_c=1250$, $H/R=1.8$. Time t in seconds is shown in the figure.

displacements are not so apparent for the initially homogeneous marker distributions. Similar to the homogeneous cases, the $c' = Ar$ case also shows marker depletion near the cylinder wall where flow separates from the wall ($t = 8$) and the formation of a marker-depleted shoulder. Although the details of the marker trajectories are different for the three different initial marker distributions, the steady-state marker-free column diameter is almost the same.

To examine the effects of marker concentration, the evolution of 19×29 markers was computed for an initially regular homogeneous distribution (Fig. 8). The evolution process is similar to that for the higher marker density 49×89 [Fig. 6(a)]; however, the final column diameter is larger for the lower concentration; the ratio of the marker-free column diameters for 19×29 and 49×89 markers is about 3.

The events that lead to the formation of the marker-free column (e.g., initiation of the flow and particle separation from the wall and the formation of shoulders) in the simulation are almost the same as those observed experimentally. Evolution of the marker-depleted shoulderlike layer observed in the experiment is shown at three time instances in Fig. 9, which depicts the region near the

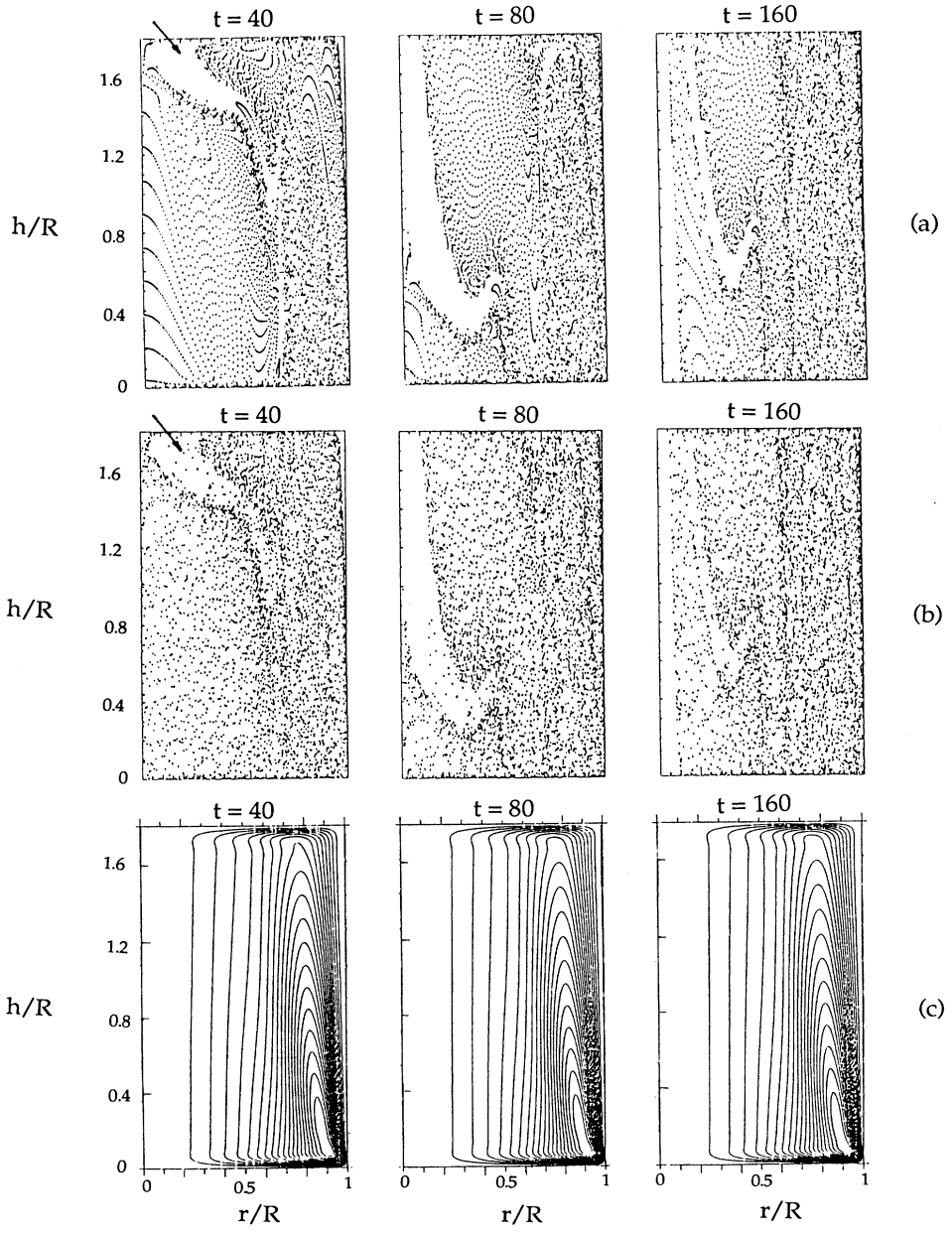

FIG. 6 *(Continued).*

top corner only. In these pictures, the white dots denote particles, while the black areas are regions that are devoid of particles.

C. Analysis of DNS results

Numerical (as well as experimental) results show that the separation process occurs near the lateral wall. If the initial near-wall clear layer thickness δ_w is increased, the amount of separated clear fluid and, hence, the diameter D of the central clear column increases. In simulations with a regular particle distribution, δ_w is also the distance ℓ between nearest particles and related to particle concentration c as

$$\delta_w = \ell = c^{-1/3} , \tag{1}$$

by considering one particle in a cube of length ℓ.

To check the accuracy of the marker positions at each time step, we computed the streamlines until steady state was reached, and then several markers were introduced near the bottom plate. Indeed, with increasing time, each particle followed its trajectory (meridional streamline) and came to its original position. This implies that no perceptible error is introduced in the integration process.

More recently, numerical studies [4] also demonstrated the formation of a vortex bubble with depleted markers. In contrast to our initial marker distribution, they introduced markers along the axis. Nevertheless, marker depletion in both cases is due to the nonuniformity of meridional streamlines and hence marker concentration.

For marker distributions corresponding to $\ell = 1/50$ as in Fig. 6(a) and $\ell = 1/20$ as in Fig. 8(a), the steady column diameters (nondimensionalized by the disk diameter) are, respectively, 0.24 and 0.6 at $t = 160$, revealing that D is related to marker concentration. This was true for both regular and random homogeneous particle distributions. The dependence of D on ℓ in the simulations is

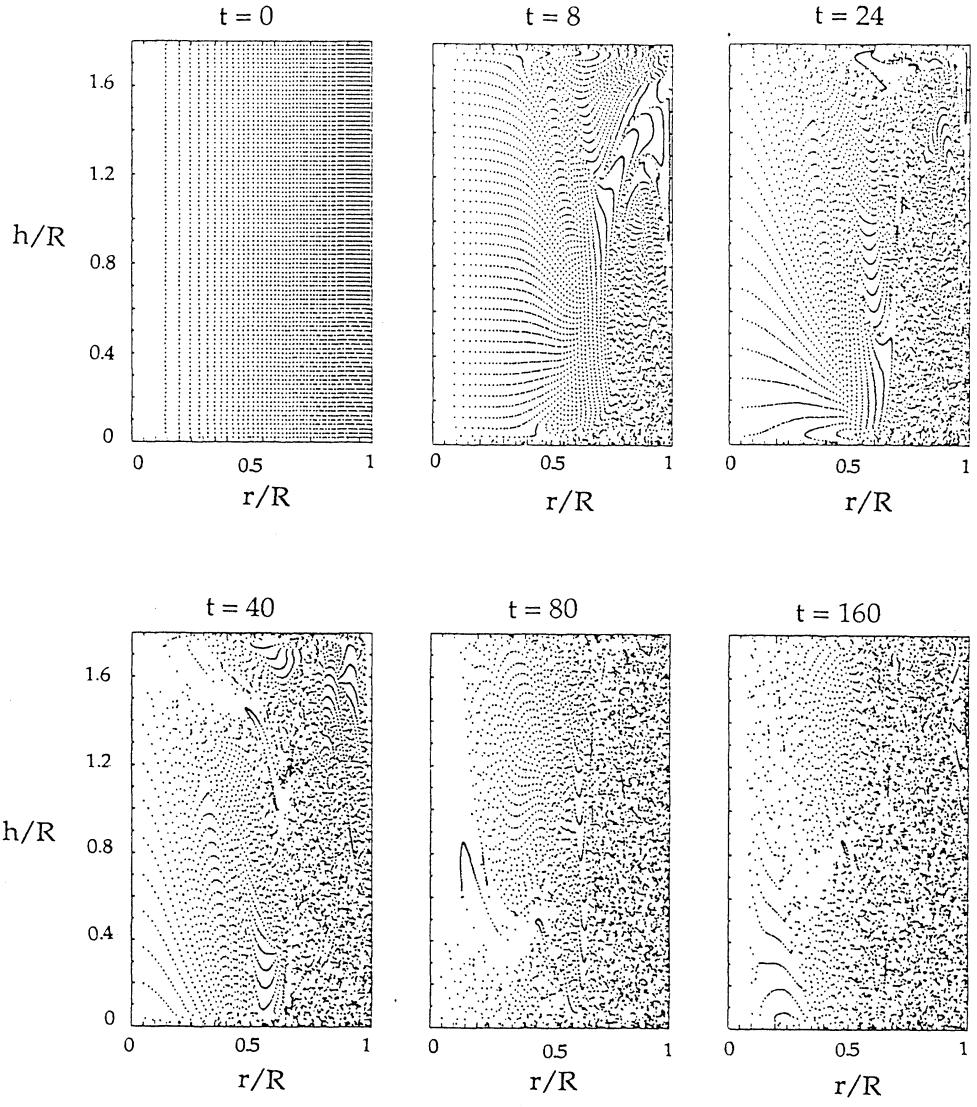

FIG. 7. Numerical simulation results showing time evolution of trajectories of 49×89 markers for initially linear distribution of markers $c' \sim r$. $\mathrm{Re}_b = 2500$, $\mathrm{Re}_c = 1250$, $H/R = 1.8$.

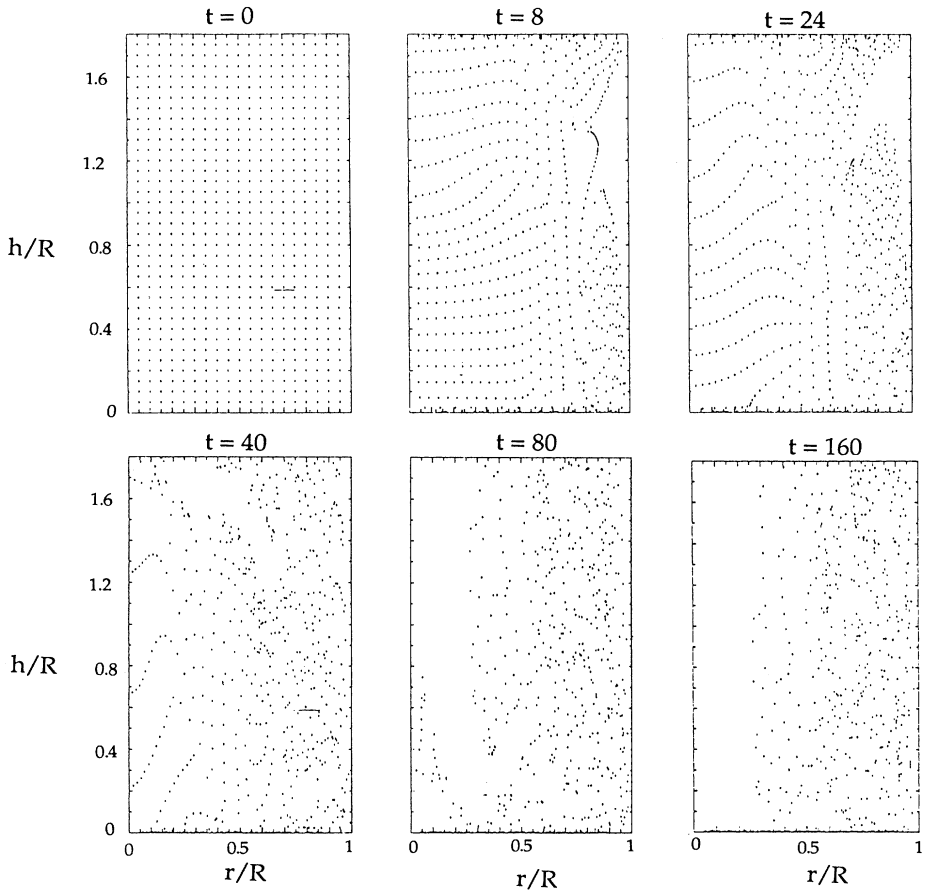

FIG. 8. Numerical simulation results showing time evolution of trajectories of 19×29 markers for initially regular homogeneous marker distribution. $Re_b = 2500$, $Re_c = 1250$, $H/R = 1.8$.

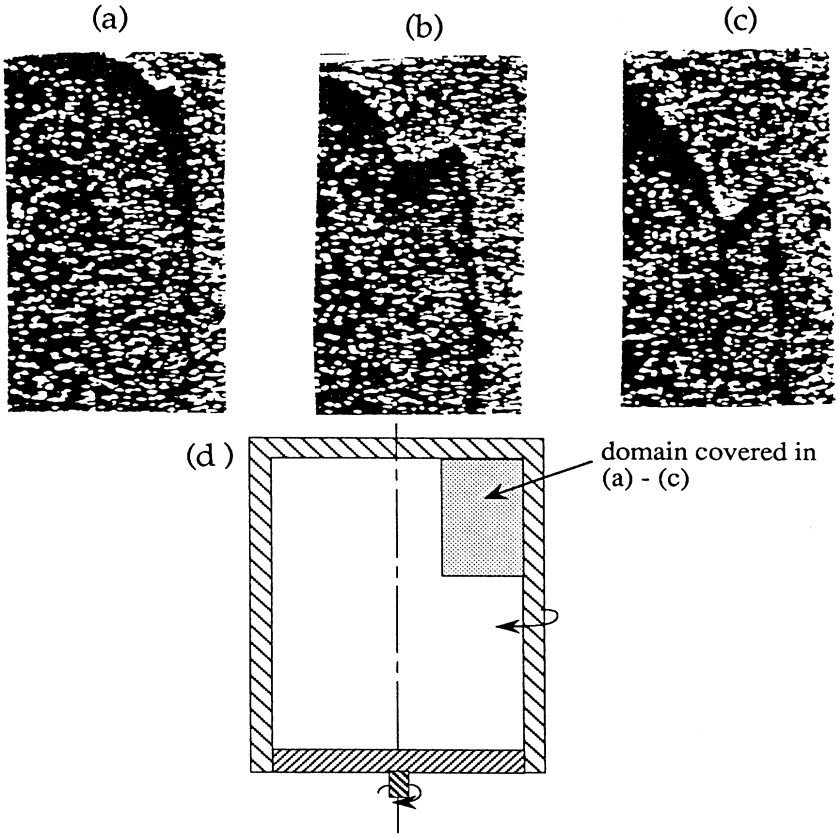

FIG. 9. Flow visualization pictures showing particle separation sequence near the corner in the case of vortex column for an initially homogeneous mixture of water and polystyrene particles (44 μm). $Re_b = 28\,800$, $Re_c = 14\,400$, $t = 30$, 45, and 60 s.

not unexpected. When the marker concentration increases, the minimum distance between the markers and the wall (δ_{min}) decreases and these near-wall markers follow streamlines closer to the axis, producing a smaller marker-free column diameter. We computed the time evolution of 19×29 markers with an initial distribution similar to that shown in Fig. 8 ($t=0$), except that the distance between the outermost layer of markers and the walls of the disk and the can was decreased. This distribution produced a smaller marker-free D than that shown in Fig. 8. These simulations confirm that D depends on the proximity of the markers to the walls; for a regular distribution, this proximity is dictated by marker concentration c, and hence D shows a dependence on c. However, in experiments, the minimum distance between the particle center and the wall is determined by its radius, not the concentration. Thus, a relevant length scale in experiments is the particle diameter d. This has been experimentally verified and is discussed in Sec. IV.

Although d is very small, our flow device acts like a kinematic amplifier of marker distance from the wall. It is clear from the meridional streamlines that when a marker advects along a streamline, its minimum distance δ_a from the axis is much greater than the minimum distance δ_{min} from the bottom wall. For VC with small values of δ_{min} and δ_a, an amplification coefficient k can be defined as

$$k=\frac{\delta_a}{\delta_{min}}=\left[\frac{r_m\omega_m}{w_m}\right]^{1/2}, \tag{2}$$

where ω_m is the maximum azimuthal vorticity at the bottom, r_m is the corresponding radius, and w_m is the maximum axial velocity on the axis. The relation in (2) is obtained by Taylor expansion (up to the third term) of a meridional stream function at two locations (e.g., close to the axis at a radial distance of δ_a and near the bottom surface at a distance δ_{min}) and by equating these two expressions.

The value of δ_{min} cannot be less than the particle radius, and D in the steady regime can be determined by the relation

$$D=kd\ . \tag{3}$$

For VB, (3) is not valid because a streamline even infinitesimally close to the bottom disk deviates from the axis on the bubble surface over a finite distance, and thus the separation region should not depend on the marker concentration. Steady-state marker distributions for initially 19×29 and 49×89 regular homogeneous markers are shown in Figs. 10(a) and 10(b). We have also performed computations for initially random marker distributions (not shown here). These results demonstrate that the final marker depleted VB size is independent of these two initial distributions and the concentrations of markers, and that the marker depleted VB is quite similar to that observed experimentally (Fig. 2).

These results for VB seem to confirm the kinematic separation hypothesis. However, this hypothesis is inadequate to explain separation for VC. Using $k=50$ (obtained from the simulation of VC) and smoke size $d=0.1$ μm, Eq. (3) leads to $D=5$ μm, which is much smaller than that observed experimentally. For experimentally observed D, δ_{min} would have to be 10^4 times the particle size. If we account for this discrepancy by considering that smoke particles sink due to gravity from the top disk during the flow establishment time (say 60 s), (A7) gives $\delta_w=21.6$ μm. Using $k=50$, we obtain $D=0.18$ mm, which is still too small. Thus, although the particle separation picture obtained via DNS is qualitatively consistent with experimental observation, quantitatively they are different. It is quite plausible that an unknown interaction between particles and the apparatus wall may have significant effects on D and must be taken into account.

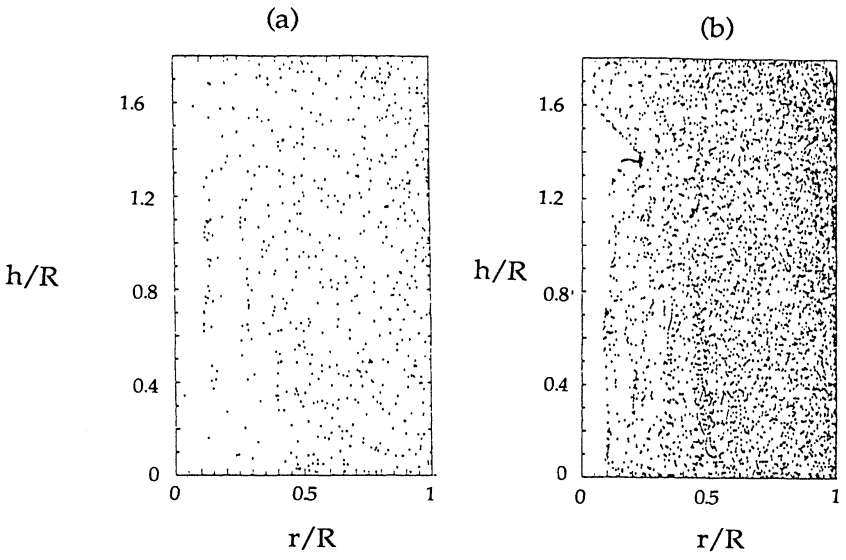

FIG. 10. Numerical simulation results showing the marker separation in a vortex breakdown bubble for initially regular-homogeneous marker distribution. (a) 19×29 markers; (b) 49×89 markers. $Re_b=2500$, $H/R=1.8$, $t=160$.

IV. QUANTITATIVE MEASUREMENT

A. Experimental approach

Our experiments with smoke-air mixtures have limitations: irregular particle shape, unknown size distribution and concentration. These are overcome by using mixtures of water and spherical polystyrene particles of various sizes (5, 10, 21, and 44 μm diameter). The dependence of D and its establishment time on particle size and concentration over a range of $(\Omega_b-\Omega_c)$ and Re_b have been quantitatively studied. Separation of 21-μm particles in alcohol and other mixtures has also been studied.

B. Experimental results

Figure 11 shows the linear dependence of the column diameter D on the particle size d for $\mathrm{Re}_b=14\,410$, $\Omega_b/\Omega_c=0.5$ and volumetric particle concentration $c_v=6.39\times10^{-6}$ [c_v=(volume of the particles)/(volume of the chamber)]. Using the minimum distance of a particle from the bottom disk as its radius, the linear dependence follows (3) with $k=1300$, a value much higher than $k=50$ given by DNS. Purely kinematic effects cannot account for this large difference, thus leading to the conclusion that there must be some unknown force repelling the particles away from the walls.

Experiments also revealed a nontrivial dependence of D on $(\Omega_b-\Omega_c)$. For a given d at a fixed Re_b, D is found to increase with decreasing $(\Omega_b-\Omega_c)$. However, for solid-body rotation, i.e., $\Omega_b-\Omega_c=0$, the particle-free column does not form. For a given Ω_b, with increasing Ω_c the meridional streamlines are increasingly concentrated near the cylinder wall and rarefied near the axis because of a stronger radial flow produced by the upper disk. Streamlines in effect move away from the axis producing a larger particle-depleted column.

Our data for various sizes of polystyrene particles in *water* as well as in *pure alcohol* and for various values of $\Omega_b-\Omega_c$ and Re_b, collapse onto a single line in the $(D^*;\Omega^*\mathrm{Re}_b^{1/2})$ coordinates (Fig. 12), where $D^*=D/d$, $\Omega^*=(\Omega_b-\Omega_c)/\Omega_b$. Data for the smoke-air mixture in these coordinates also collapse but onto a different line. In addition to a jump between these two cases, the variation in the smoke-air case is higher than that in the water-particle case. The reason for this jump is unclear. However, the collapse of data onto a single line for spherical polystyrene particles in the two separate media, e.g., water and alcohol, and the collapse of data for irregular cornflakelike smoke particles onto a different line indicate that the jump may be related to the shape of smoke particles. Note that the dependence of D^* on $\mathrm{Re}_b^{1/2}$ indicates that the boundary layer characteristics play an important role.

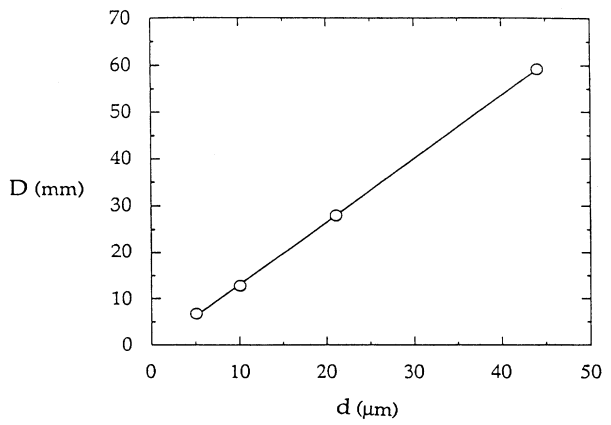

FIG. 11. Dependence of the column diameter D (in mm) on particle size. $\mathrm{Re}_b=14\,410$, $\Omega_b/\Omega_c=0.5$.

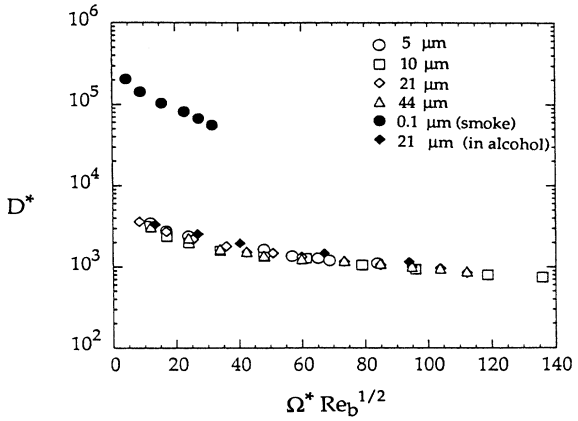

FIG. 12. Dependence of nondimensional column diameter D^* $(\equiv D/d)$ on $\Omega^*\mathrm{Re}_b^{1/2}$.

With decreasing values of $\Omega_b-\Omega_c$, the particle-free column establishment time increases as $t\sim1/(\Omega_b-\Omega_c)$ because of the decrease in the meridional flow in the vortex core region. The establishment time of the steady particle-free column is determined by the time at which the leading edge of the descending column reaches the bottom disk. Experimental data collapse well in the nondimensional coordinates $[t(\Omega_b-\Omega_c);\mathrm{Re}_b^{1/2}]$, as is shown in Fig. 13. This dependence can be expressed as

$$t=2\mathrm{Re}_b^{1/2}(\Omega_b-\Omega_c)^{-1}\,. \tag{4}$$

The time t increases with Re_b and decreases with increasing velocity difference $(\Omega_b-\Omega_c)$. For example, when $\mathrm{Re}_b=2500$ and $\Omega_b-\Omega_c=3.23$ rad/s, (4) yields

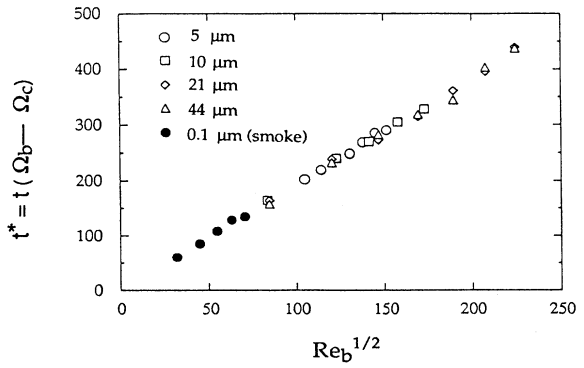

FIG. 13. Dependence of the particle-free column establishment time $t^*=t(\Omega_b-\Omega_c)$ on Re_b.

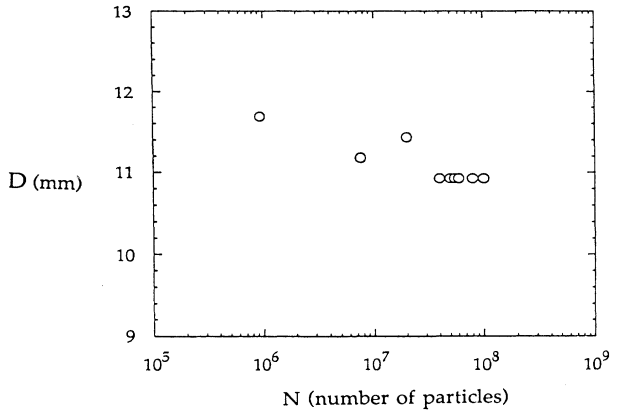

FIG. 14. Dependence of column diameter D (in mm) on particle concentration. $Re_b = 28\,820$, $\Omega_b/\Omega_c = 0.5$, $H/R = 1.125$, 10-μm particles.

$t = 31$ s, which is comparable to the flow establishment time.

Note that, unlike the column diameter, the column establishment time data for smoke and polystyrene particles collapse onto a single line. This is due to the establishment time being a characteristic not of the separation phenomenon, but of the kinematics of the flow where particles are frozen to the flow irrespective of their shapes.

The influence of particle concentration is shown in Fig. 14 for 10-μm particles at $Re_b = 14\,410$ and $\Omega^* = 0.5$. The column diameter D shows no significant variation even with a 100-fold increase in the particle concentration. This is consistent with the fact that, in laboratory experiments, the smallest distance between the particles and the walls depends only on d, and hence D depends on d, not on c_v.

C. Some striking observations

1. Concentration

Although particle concentration within a certain range had no obvious effect on particle-free column diameter (Fig. 14), further increase in the particle concentration led to an initially axisymmetric column which first became unsteady and subsequently asymmetric. Figures 15(a)–15(c) show schematically the development of asymmetry with increasing particle concentration (shaded regions represent column cross section). Figure 15(a) shows an axisymmetric column at low particle concentration. At a higher particle concentration, the column becomes asymmetric [Fig. 15(b)]. When the particle concentration is increased further, the initial circular cross section became ellipticlike, then dumbbell shaped, and finally S shaped. Figure 15(c) shows instantaneous column cross sections at different heights. For still higher particle concentration, the column first becomes asymmetric as shown in Fig. 15(b) and then its cross section starts deforming. The cross section is then elongated in the azimuthal as well as radial directions until the thin particle-free regions can no longer be identified. Time evolution of the cross section at approximately the midheight of the column is schematically shown in Figs. 16(a)–16(k). After the disappearance of the sheared column, a new particle-free column appears after descending from the top; the sequence just described is repeated then, and so on.

These results are indeed surprising. An increase in the particle concentration should increase the effective viscosity (according to Einstein's formula), thereby decreasing the effective Reynolds number. In this case, it is natural to expect a more stable state, contrary to the opposite effect observed.

A systematic study was performed using a known number of polystyrene particles in water for various values of Re_d and Ω^*. Experiments revealed that the loss of symmetry of the particle-free column depends on volumetric particle concentration c_v and the parameter $\Omega^*(Re_d)^{1/2}$. For 5-, 10-, and 21-μm polystyrene particles, loss of axial symmetry of the column occurred when c_v reached a value of about 3.4×10^{-5} when $\Omega^*(Re_d)^{1/2} \approx 120$, irrespective of particle size. With decreasing $\Omega^*(Re_d)^{1/2}$, a higher c_v was needed for initiation of column symmetry breaking. For example, when $\Omega^*(Re_d)^{1/2} = 105$, asymmetry occurred for $c_v \approx 5.1\times10^{-4}$. Symmetry breaking could not be observed for $\Omega^*(Re_d)^{1/2} \leq 100$ since the re-

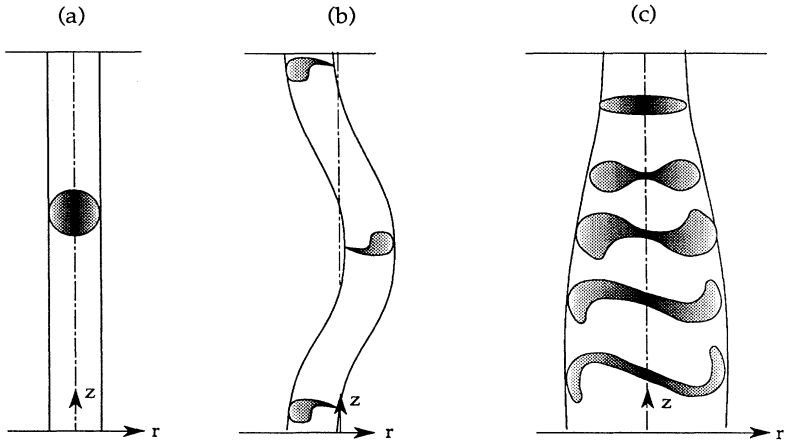

FIG. 15. Effects of particle concentration on the development of the particle-free vortex column shown schematically. (a) Low concentration, (b) moderate concentration, (c) high concentration.

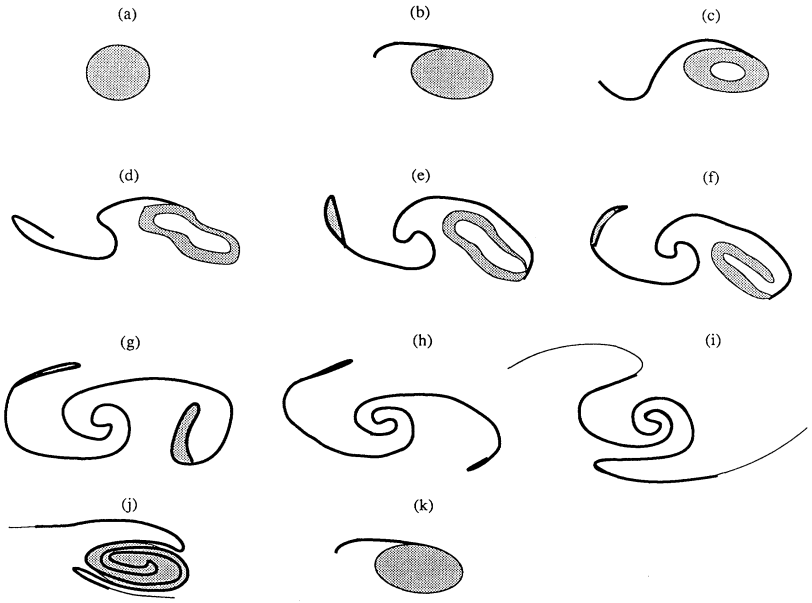

FIG. 16. Schematics showing the time evolution of particle-free column cross section for particle concentration higher than the case in Fig. 15(c).

quired increased particle concentration caused insufficient contrast for visualization due to intense particle scattering. Since the size of smoke particles is at least an order of magnitude smaller than the polystyrene particles, symmetry breaking of the column for the smoke-air mixture could be observed even at $\Omega^*(\mathrm{Re}_d)^{1/2}\approx 20$. However, in the smoke-air case, the value of c_v is unknown.

The observed unsteadiness and symmetry breaking of the column is not the effect of high values of Re_d or Ω^*, as revealed by visualization using fluorescent dye in pure water or water with a low particle concentration. This experiment was performed for $\Omega^*(\mathrm{Re}_d)^{1/2}\leq 160$ (because of the speed limitations of the facility) and within this range, the column remained steady.

Recall that the particle-free column diameter D depends on the parameter $\Omega^*(\mathrm{Re}_d)^{1/2}$ (see Fig. 12); a lower $\Omega^*(\mathrm{Re}_d)^{1/2}$ produces a larger column diameter. The observed dependence of the symmetry breaking on $\Omega^*(\mathrm{Re}_d)^{1/2}$ indicates that a smaller diameter column is prone to become unstable for a smaller particle volume fraction. This suggests that the slenderness ratio H/D is a pertinent parameter to initiate symmetry breaking. The mechanism that produces asymmetry at high particle concentrations and the role of H/D need further study.

2. *Fluid composition*

The polystyrene particles have a specific gravity of 1.04. For water, if we use $\nu=10^{-6}$ m^2/s and $\rho=1$ g/cm^3, (A7) gives the terminal sedimentation velocity $w_g=5.45\times10^{-7}$ and 4.2×10^{-5} m/s for the 5- and 44-μm particles, respectively. These values of w_g are too small to explain the establishment of a particle-free column within about 60 s. But to eliminate even this small difference in density, small quantities (see below) of sugar were added to increase the specific gravity of the sugar-water solution. After each addition, the water, sugar, and particles were thoroughly mixed by rotating the disk and the can in opposite directions. Figure 17(a) is for pure water and Figs. 17(b) and 17(c) are for the water-sugar solution, all with 10-μm particles; specific gravities of the sugar-water solution for the cases shown in Figs. 17(b) and 17(c) were 1.0016 and 1.0033, respectively. Figures 17(a)–17(c) show that, with addition of a small amount of sugar, the particle-free column diameter is, at first, reduced considerably [Fig. 17(b)], and then the column loses its axial symmetry [Fig. 17(c)]. The particle-free column disappeared completely when the sugar-water solution specific gravity reached about 1.01, which is still noticeably lower than that of the poly-

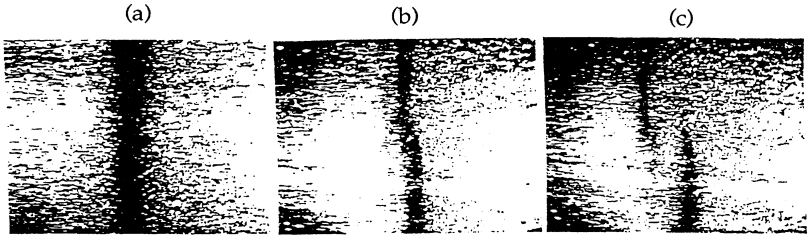

FIG. 17. 10-μm polystyrene particle separation in water and effects of additive (sugar). (a) in water; (b) in water-sugar solution, specific gravity = 1.002; (c) in water-sugar solution, specific gravity = 1.005. $\mathrm{Re}_b=28\,820$, $\Omega_b/\Omega_c=0.5$.

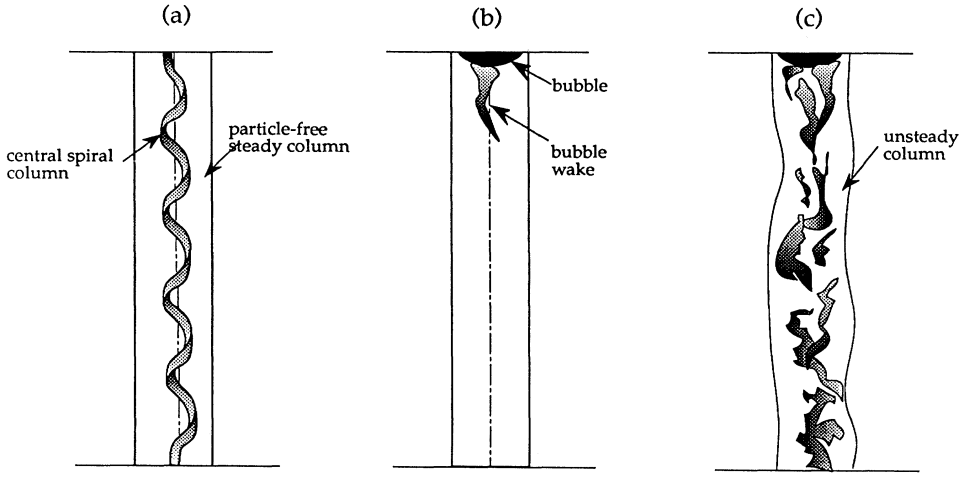

FIG. 18. Schematics showing the effects of additive on the flow instability observed by fluorescent dye streak. (a) Water; (b),(c) water and solute.

styrene particles.

Similar results, e.g., reduction in the particle-free column diameter, loss of axial symmetry, and finally complete disappearance of the column were observed by increasing specific gravity by adding salt instead of sugar and even when the specific gravity was lowered by adding ethyl alcohol (specific gravity 0.789). However, when we used pure alcohol instead of a water-alcohol solution, separation of particles in alcohol occurred as in pure water. The effect observed for both increasing or decreasing specific gravity of the solution implies that specific gravity of the particles is not the cause of unsteadiness. Even for the air-smoke mixture, adding alcohol vapor (typically from 2–3 drops, which is negligible by volume) in the flow chamber revealed the same sequence of anomalous events as observed when adding sugar or salt in water-polystyrene particle mixture.

In all of these cases, the amount of additive and the corresponding change in the kinematic viscosity of the water-additive mixture were small; thus the effect due to changes in the Reynolds number should be negligible. Furthermore, the formation of a particle-free column was observed over a wide range of Reynolds numbers (1000–5000 using air and 7000–57 000 using water). A small change in the Reynolds number (due to a small amount of additive) is not expected to affect the flow. However, it appears that additives change the dynamics of the flow within a region near the axis.

We examined the cause of flow unsteadiness via visualization by allowing a drop of fluorescent dye to seep through a small hole at the center of the top disk such that the flow is not disturbed. The effect of the solute on the column is schematically shown in Figs. 18(a)–18(c). For pure water, a steady spiral central column marked by the fluorescent dye is observed [Fig. 18(a)]. However, for the water-sugar or water-alcohol solution, a hemispherical bubble formed at the top center; the injected dye remains trapped inside the bubble. The converging meridional streamlines are disturbed as they pass around the bubble and descend downward. During this process, a small amount of dye from the bubble diffuses and advects downstream [Figs. 18(b) and 18(c)]. The disturbed flow downstream of the bubble presumably induces the unsteadiness and asymmetry of the particle-free central column. For a given set of H/R, Re_d, and Ω^*, one would expect the flow to be the same irrespective of the fluid composition. However, our experiment shows a surprising dependence on fluid composition (i.e., formation of a bubble).

V. CONCLUSIONS

The "antidiffusion" phenomenon is manifested in the spontaneous separation of components of an initially uniform mixture in a simple rotating device. The fluid velocity in this device is so small that particle separation within a short time (on the order of tens of seconds) cannot be explained by the action of known forces acting on the particles. The purely kinematic explanation of this phenomenon, considered in Ref. [2], is partially confirmed by numerical simulation of *massless* marker trajectories and by experiments that demonstrate that the particle-marker-free column size increases with increasing distance between the particles-markers and the wall.

Experimentally, this phenomenon can be explained in the kinematic frame by viewing our device as a hydrodynamic amplifier and considering the finite size of real particles, where a particle very close to the bottom disk is displaced through a large transverse distance from the axis. However, this effect is not explained quantitatively, though the diameter D is found experimentally to increase proportionately to the particle size consistent with the kinematic explanation. The experimentally observed amplification coefficient for particles is much greater than that obtained for markers via numerical simulations. The higher value of k observed experimentally may also be a result of a significant unknown repelling force acting on the particles near the walls.

A strong dependence of the flow on the fluid mixture composition is extremely enigmatic. Small amounts of an additive (sugar, salt, or alcohol in water, alcohol vapor in air) make the flow unsteady, resulting in symmetry breaking of the particle-free column, and finally, total disappearance of the column. The influence of fluid composition is very surprising because the solutions are Newtonian fluids, which are characterized by two parameters

only: density and viscosity. But our experiments show evidence of a third parameter—the solution composition.

ACKNOWLEDGMENTS

The authors are grateful to Wei Wu for performing the numerical simulations and to Scott Simons for a careful review of the manuscript. This work was supported by the Office of Naval Research Grant No. N00014-89-J-1361 and the National Science Foundation Grant No. SGER-9122746.

APPENDIX A: FORCES ACTING ON PARTICLES

1. Identification of forces

Consider the flow of a fluid-particle mixture with a very small volumetric particle concentration. Thus the interparticle distance is so large that the interaction between particles can be neglected and the particles considered isolated.

Gravity and inertial forces depend on particle density ρ_p and are proportional to d^3 (d being the effective particle diameter). This is also valid for forces related to pressure gradient, e.g., buoyancy force.

An expression for the viscous interaction body forces typically assumes the functional dependence

$$\vec{f}=\vec{f}(\vec{v}-\vec{w},\mathsf{D},\nabla\cdot\mathsf{D}) , \tag{A1}$$

where $\vec{v}$ is the fluid velocity, $\vec{w}$ is the particle center velocity, and D is the fluid deformation tensor, e.g., the symmetric part of grad $\vec{v}$. Passman [5] used the representation

$$\begin{aligned}\vec{f}&=\beta_1(\vec{v}-\vec{w})+\beta_2\mathsf{D}(\vec{v}-\vec{w})+\beta_3\nabla\cdot\mathsf{D}+\beta_4\mathsf{D}\nabla\cdot\mathsf{D} ,\\ &=f_1+f_2+f_3+f_4 ,\end{aligned} \tag{A2}$$

which contains the expressions employed by McTigue, Givler, and Nunziato [6]. Terms appearing in this expression are associated with Stokes drag [7], Safman lift [8], Faxen force [7], and Ho-Leal lift [9]. Coefficients are determined from an approximate solution of the Navier-Stokes equations. These coefficients are typically functions of fluid density ρ, viscosity μ, $\mathrm{Tr}\mathsf{D}$, $|\nabla\cdot\mathsf{D}|$, and characteristic particle size d (for an incompressible fluid $\mathrm{Tr}\mathsf{D}=0$).

The expression of Stokes drag for a spherical particle is well known [10]:

$$\vec{f}_1=3\pi\mu d(\vec{v}-\vec{w}) . \tag{A3}$$

The magnitude of the Saffman lift force [8] is

$$f_2=1.62\rho(v-w)d^2(\kappa\nu)^{1/2} , \tag{A4}$$

where κ is the magnitude of velocity gradient and $\nu=\mu/\rho$ is the kinematic viscosity. [We are not sure if the second term in (A2) is a relevant representation of (A4)]. A comparison of (A2), (A3), and (A4) shows that $f_1\sim d$ and $f_2\sim d^2$. It can also be shown that $f_3\sim d^3$ [7] and $f_4\sim d^4$ [9].

It is worthwhile to mention that the Basset force f_B [7], associated with the relative acceleration of a particle, is proportional to d^2, and the Magnus lift force f_M due to particle swirl is proportional to d^3. According to Rubinov and Keller [11], the Magnus force for small Reynolds numbers can be expressed as

$$\vec{f}_M=\tfrac{1}{8}\pi d^3\rho\vec{\Omega}\times(\vec{v}-\vec{w}) , \tag{A5}$$

where Ω is the angular velocity of the particle. Note that f_M does not depend on viscosity, indicating that for small Reynolds numbers (which correspond to large ν) $f_M \ll f_2$, and hence the Magnus lift (A5) is insignificant.

Since d is very small in our case, the dominant force acting on the particle is f_1, and we will compare other forces with f_1. Consider the ratio

$$\frac{f_1}{f_2}=\frac{5.8}{d}\left[\frac{\nu}{\kappa}\right]^{1/2} . \tag{A6}$$

For practical values of d, ν, and κ, $f_1 \gg f_2$. Nevertheless $\vec{f}_2$, being normal to $\vec{f}_1$, can be important in our case.

2. Evaluation of forces

We now examine the forces acting on the particles in our apparatus in the parameter range of separation of smoke from air (Fig. 3): $R=0.0762$ m, $H=0.1397$ m, $\nu=15\times10^{-6}$ m^2/s, $\Omega_b=6.46$ rad/s, and $\Omega_c=3.23$ rad/s. The maximum centrifugal acceleration $a_c\sim0.32g$ occurs at the rim of the disk for both VB and VC, where g is acceleration due to gravity. The meridional acceleration a_m near the bottom corner of the flow device where meridional streamlines strongly converge [see Fig. 6(c)] can be estimated as $a_m=u^2/\delta$, where u is the local particle velocity and δ is the boundary layer thickness. For the disk, the Von Karman solution gives the maximum value of $u=0.2\Omega_b R\sim0.1$ m/s (see, for example, Ref. [12]). Since $\delta=R/\mathrm{Re}_b^{1/2}\approx1.52$ mm, we have $a_m\approx0.64g$. Thus for our experiments, the acceleration is on the order of g.

Experiments reveal that although kinematic separation is present and results in the formation of particle-depleted column, it is not sufficient to produce such a large D. This observation suggests a significant lateral force that repels the particles away from the walls, thus amplifying the particle-free fluid layer that accumulates in the vortex core.

The first candidate for the lateral force is gravity near the top. Using the Stokes formula (A3), we obtain the sedimentation velocity

$$w_g=\frac{1}{18}d^2\frac{g}{\nu}\frac{\rho_p-\rho}{\rho} . \tag{A7}$$

For smoke particles of $d=0.1$ μm and $\rho_p/\rho=1000$, $\nu=15\times10^{-6}$ m^2/s for air, $w_g=3.6\times10^{-7}$ m/s. The corresponding Reynolds number based on the particle diameter is 2.4×10^{-9}, guaranteeing the validity of Stokes law. In this case, the time needed for particle depletion from a volume τ near the top is $t=\tau/\pi R^2 w_g$. If we assume that the sedimentation-produced clear fluid near the top is advected toward the column core by meridional motion to produce the particle-free column, we can estimate the

column formation time. For the case shown in Fig. 3(b), the volume τ of the particle-free column is about 2% of the total flow volume. Creation of this volume of particle-free fluid by sedimentation would require $t \sim 2.2$ h; but the column is established within $t \sim 50-60$ s. Thus, gravity and centrifugal forces do not play any significant role.

Since Basset and Faxen forces act in the streamwise direction near the wall, we only consider the Saffman force f_2 and the Ho-Leal force f_4. First we consider f_2 acting on a particle near the vertical wall. We assume that the relative velocity $(\vec{v}-\vec{w})$ arises due to gravity. Thus $\vec{v}-\vec{w}$ in (A4) has to be equal to w_g in (A7). To estimate κ, we assume that the maximum velocity gradient in the flow occurs at the bottom disk rim, and we obtain κ $(\equiv du/dn) \sim u/\delta = 66\ \mathrm{s}^{-1}$. We also assume that f_2 is in equilibrium with the force due to its radial velocity w_r. Thus, instead of $\vec{v}-\vec{w}$ in (A3) we use w_r. Comparison of (A3) and (A4) yields

$$w_r = 0.172 w_g d \left[\frac{\kappa}{\nu}\right]^{1/2} = 1.3\times 10^{-11}\ \mathrm{m/s}\ . \tag{A8}$$

With this velocity, a particle would take about 2 h to move through a distance of d. Such a small value of w_r is related to a very small relative velocity w_g.

The Ho-Leal force f_4, on the other hand, does not depend on $\vec{v}-\vec{w}$ and is determined only by flow deformation (which is not small) and interaction with the boundaries. In our notation, the Ho-Leal formula can be expressed as

$$w_r = \frac{u^2}{6\pi\nu}\left[\frac{d}{R}\right]^3 G(s)\ , \tag{A9}$$

where $s = y/R$ and y is the distance from the wall. The function $G(s)$ is given numerically. Near the wall of a pipe flow, we obtain $G \approx 19.2\ \mathrm{s}^{-1/2}$ for small s and since $G \to \infty$ for $s \to 0$, a particle on the wall experiences a large repelling force. However, if we consider a particle whose center is at a distance $d/2$ from the wall (i.e., the particle is touching the wall), $w_r = 1.9\times 10^{-12}$ m/s. This velocity is almost of the same order of magnitude as in (A8), and these estimates of w_r and w_g provide the upper bound of velocities, especially if one takes into account that the Saffman force decreases closer to the wall [13].

Leighton and Acrivos [14] analyzed the lift L on a small sphere of diameter d touching a plane in the presence of a simple shear γ and found

$$L \cong 2.3(\dot{\gamma}\mu d^2)(\dot{\gamma} d^2/\nu)\ , \tag{A10}$$

which is proportional to d^4. Equating this lift with the Stokes force provides transverse particle velocity on the order of 10^{-11} m/s for $d = 1$ mm. Transverse velocity of this magnitude would require several thousand hours to form the particle-depleted volume observed.

Thus we conclude that known hydrodynamic forces are not strong enough to cause the experimentally observed particle separation.

APPENDIX B: NUMERICAL SIMULATION

1. Flow field and marker trajectories

The flow is simulated by considering a cylinder of radius R and height H. The bottom disk is rotated at a constant angular velocity Ω_b while the cylinder along with the top disk is rotated at Ω_c in the same direction. Time and length are nondimensionalized by Ω_b and R, respectively.

The flow is assumed to be axisymmetric and, therefore, the equations for ξ $(\equiv r v_\theta)$, η $(\equiv \omega_\theta/r)$ are solved in the cylindrical coordinates (r,θ,z):

$$\frac{\partial\xi}{\partial t} + v_r\frac{\partial\xi}{\partial r} + v_z\frac{\partial\xi}{\partial z} = \frac{1}{\mathrm{Re}_b}\left[\frac{\partial^2\xi}{\partial z^2} + \frac{\partial^2\xi}{\partial r^2} - \frac{1}{r}\frac{\partial\xi}{\partial r}\right]\ , \tag{B1}$$

$$\frac{\partial\eta}{\partial t} + v_r\frac{\partial\eta}{\partial r} + v_z\frac{\partial\eta}{\partial z} = \frac{1}{r^4}\frac{\partial\xi^2}{\partial z} + \frac{1}{\mathrm{Re}_b}\left[\frac{\partial^2\eta}{\partial r^2} + \frac{3}{r}\frac{\partial\eta}{\partial r} + \frac{\partial^2\eta}{\partial z^2}\right]\ , \tag{B2}$$

where $\mathrm{Re}_b = \Omega_b R^2/\nu$, the Reynolds number of the disk.

In addition, we solve Poisson equation,

$$-r^2\eta = \frac{\partial^2\psi}{\partial z^2} + \frac{\partial^2\psi}{\partial r^2} - \frac{1}{r}\frac{\partial\psi}{\partial r}\ , \tag{B3}$$

which relates the meridional stream function ψ with η, where ψ is defined such that

$$v_r = -\frac{1}{r}\frac{\partial\psi}{\partial z}\ ,\quad v_z = \frac{1}{r}\frac{\partial\psi}{\partial r}\ . \tag{B4}$$

The boundary conditions we used are as follows. $\psi=0$, $\xi=0$:

$$\frac{\partial\eta}{\partial r} = 0\quad (r=0,\ 0<z<H/R)\ ; \tag{B5}$$

$\psi=0$, $\xi=C$:

$$\eta = -\frac{\partial^2\psi}{\partial r^2}\quad (r=1,\ 0<z<H/R)\ ; \tag{B6}$$

$\psi=0$, $\xi=r^2$:

$$\eta = -\frac{1}{r^2}\frac{\partial^2\psi}{\partial z^2}\quad (z=0,\ 0<r<1)\ ; \tag{B7}$$

and $\psi=0$, $\xi=Cr^2$:

$$\eta = -\frac{1}{r^2}\frac{\partial^2\psi}{\partial z^2}\quad (z=H/R,\ 0<r<1)\ . \tag{B8}$$

We used a fourth-order-accurate compact differencing scheme for spatial derivatives on a 200×360 grid and a fourth-order Runge-Kutta scheme for time differencing.

From the velocities $v_r = dr/dt$ and $v_z = dz/dt$, the marker position (r,z) was calculated using the fourth-order Runge-Kutta scheme, while its velocity at the new location was computed by an area-weighting method. To achieve a high accuracy in high-velocity gradient regions near the boundaries, a fourth-order-accurate interpolation scheme was used.

2. Initial marker distribution

We select N massless markers and assign their initial positions to obtain a "uniform" distribution. The concept of a uniform distribution in the case of a discrete set of markers is nontrivial. To obtain a "uniform" distribution, we can, for example, divide the flow domain into small cubes, placing one marker at the center of each cube; this corresponds to a regular homogeneous marker distribution. On the other hand, a random, homogeneous marker distribution can be obtained by placing each marker at a random location inside each cube. However, such a description of an initially uniform distribution is not convenient for our case. First, it is impossible to divide a cylindrical volume into regular cubes. Second, for an axisymmetric flow, such marker distributions will produce three-dimensional trajectories, requiring a long computational time. Thus we devised a simplified model that uses a small number of markers to simulate experiments with a considerably larger number of particles.

To simplify the problem, we consider the motion of markers in the meridional plane, which is divided into a square grid. For the axisymmetric case, the particle trajectories can be obtained from the system of equations:

$$\frac{dr}{dt}=v_r(r,z,t)\ , \quad \frac{dz}{dt}=v_z(r,z,t)\ , \quad \frac{d\theta}{dt}=\frac{1}{r}v_\theta(r,z,t)\ , \tag{B9}$$

where (r,z,θ) are cylindrical coordinates and t is time. It is sufficient to solve only the first two equations, which form a closed system for the axisymmetric velocity field (v_r,v_z,v_θ). This approach allows the values of r and z to be considered, not as the real marker locations in cylindrical coordinates, but rather their cylindrical projections onto the meridional plane (r,z). In this case, it is possible to formulate a two-dimensional problem considering (r,z) as Cartesian coordinates to describe the motion of markers in the meridional plane. However, if we consider a random but homogeneous volume distribution of material particles with concentration c (number of particles per unit volume), this distribution corresponds to a nonuniform distribution in the (r,z) plane with concentration c' (number of particles per unit area).

For the continuum case, the transport equation

$$\frac{\partial c}{\partial t}+\mathrm{div}cv=0 \tag{B10}$$

leads to $c=$const for a 3D incompressible flow ($\mathrm{div}v=0$). But if we consider the axisymmetric flow as a planar flow with velocity components v_r and v_z, then

$$\frac{\partial v_r}{\partial r}+\frac{\partial v_z}{\partial z}=-\frac{v_r}{r}\neq 0\ .$$

For the planar concentration c', (B10) can be written as

$$\frac{\partial c'}{\partial t}+v_r\frac{\partial c'}{\partial r}+v_z\frac{\partial c'}{\partial z}=\frac{v_r}{r}c'\ . \tag{B11}$$

This equation is satisfied by $c'=Ar$, where $A=$const. Thus, the distribution $c'=Ar$ in the meridional plane corresponds to a uniform distribution $c=$const in space.

The physical meaning of these distributions is as follows. For a homogeneous distribution of particles in the cylindrical volume, the number of markers in a cylindrical layer of thickness dr at a radius r_2 will be more than that in an inner layer at r_1 $(r_2>r_1)$. Since the perimeter of the layer is proportional to r, the number of projected particles ($r=$const) on the meridional plane will increase proportionately, i.e., $c'\sim r$. Such a linear distribution does not correspond to the experimental situation where the uniform space distribution corresponds to a uniform distribution in the laser sheet. The particles seen in the laser sheet are due to the presence of particles in the laser sheet, not the projections of out-of-plane particles.

To avoid this difference, we describe an alternative distribution. Consider a ring layer of thickness dr and height dz, and n markers with radial coordinates r_i, where each marker is placed in a cell of length dl in the θ direction. If the coordinates r_i are all different, projection of the ring onto the meridional cell $drdz$ will contain n points. But if r_i are all equal, the projection of all markers will coincide at a single point. In this case, a homogeneous volume distribution corresponds to a homogeneous distribution on the meridional (r,z) plane, and the position of the markers within the meridional cell $drdz$ can be random. Thus, the simplest mathematical model, contrary to the real situation, considers a not quite random marker distribution in the device. Note that, for such a projection method, the number of markers per unit area should satisfy (B11) without the right-hand side, i.e., Eq. (B10) for the axisymmetric case, and one can suggest that $c'\sim c$. Also note that such a projection method is valid only for markers, not for real particles having mass.

[1] M. Goldshtik, H. S. Husain, and F. Hussain, Nature **357**, 141 (1992).

[2] M. Goldshtik, H. S. Husain, and F. Hussain, Phys. Rev. A **45**, 8611 (1992).

[3] J. Feng, H. H. Hu, and D. D. Jospeh, J. Fluid Mech. **277**, 271 (1994).

[4] J. N. Sorensen and E. A. Chrintensen, Phys. Fluids **7**, 764 (1995).

[5] S. L. Passman, J. Rheol. **30**, 1077 (1986).

[6] D. F. McTigue, R. C. Givler, and J. W. Nunziato, J. Rheol. **30**, 1053 (1986).

[7] J. Happel and H. Brenner, *Low Reynolds Number Hydrodynamics* (Prentice-Hall, Englewood Cliffs, NJ, 1965).

[8] P. G. Saffman, J. Fluid Mech. **22**, 385 (1965).

[9] B. P. Ho and L. G. Leal, J. Fluid Mech. **65**, 365 (1974).

[10] G. K. Batchelor, *An Introduction to Fluid Mechanics* (Cambridge University Press, Cambridge, 1967).

[11] S. I. Rubinov and J. B. Keller, J. Fluid Mech. **11**, 447 (1961).

[12] H. Schlichting, *Boundary Layer Theory* (McGraw-Hill, New York, 1968).

[13] J. B. McLaughlin, J. Fluid Mech. **246**, 249 (1993).

[14] D. Leighton and A. Acrivos, J. Appl. Math. Phys. **36**, 174 (1985).